

LET-3D-AP: Longitudinal Error Tolerant 3D Average Precision for Camera-Only 3D Detection

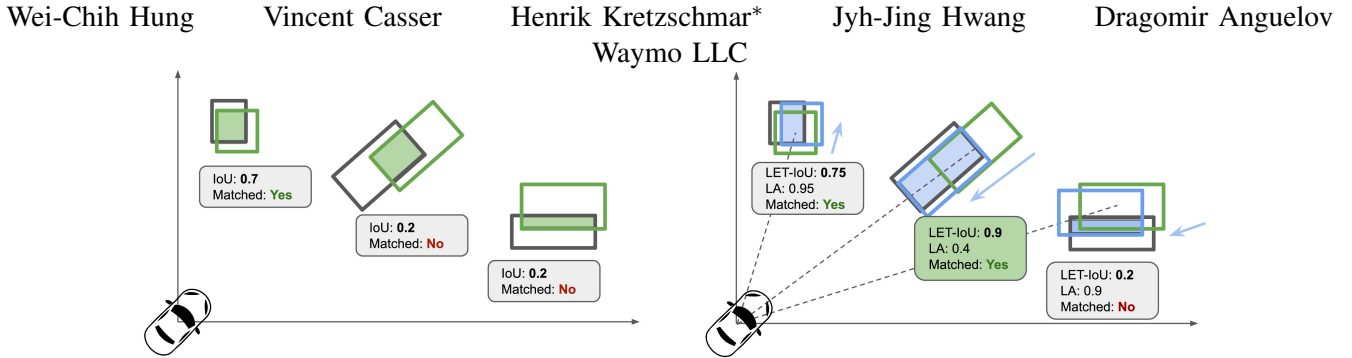


Fig. 1. Evaluating camera-only 3D detections when using the 3D Average Precision (3DAP) metric (left) and when using the proposed longitudinal error tolerant, LET-3D-AP(L) metric (right). The figures depict the bipartite matching between the detections (green) and the ground truth objects (black). Regular 3D AP matching (left) is based on the intersection over union (IoU) values and cannot match the detections that suffer from longitudinal localization errors, though the detection is reasonable and can provide useful signals to down stream modules. In contrast to this, the proposed LET-3D-AP(L), shown on the right, is more permissive by shifting the predictions to mitigate the longitudinal localization errors. We show the shifted predictions in blue, which are used for computing the longitudinal error tolerant intersection over union (LET-IoU). To account for the used longitudinal tolerance, we propose longitudinal affinity (LA) as a measure of how close the original prediction is to the ground truth in the longitudinal direction.

Abstract—The 3D Average Precision (3DAP) relies on the intersection over union between predictions and ground truth objects. However, camera-only detectors have limited depth accuracy, which may cause otherwise reasonable predictions that suffer from such longitudinal localization errors to be treated as false positives. We therefore propose variants of the 3D AP metric to be more permissive with respect to depth estimation errors. Specifically, our novel longitudinal error tolerant metrics, LET-3D-AP and LET-3D-APL, allow longitudinal localization errors of the prediction boxes up to a given tolerance. To evaluate the proposed metrics, we also construct a new test set for the Waymo Open Dataset, tailored to camera-only 3D detection methods. Surprisingly, we find that state-of-the-art camera-based detectors can outperform popular LiDAR-based detectors with our new metrics past at 10% depth error tolerance, suggesting that existing camera-based detectors already have the potential to surpass LiDAR-based detectors in downstream applications. We believe the proposed metrics and the new benchmark dataset will facilitate advances in the field of camera-only 3D detection by providing more informative signals that can better indicate the system-level performance. *

I. INTRODUCTION

Detecting objects in 3D space is a fundamental task in many robotics applications, including autonomous driving, unmanned aerial vehicles, robot navigation, and augmented reality. While LiDAR-based object detection [1]–[7] has been studied extensively in recent years with impressive results, reliable camera-based 3D object detection remains a challenging and active area of research [8]–[20].

According to common metrics, LiDAR-based detectors outperform camera-based detectors by a large margin, suggesting that camera-based object detectors fail to detect many objects. However, a careful evaluation of the failure cases reveals that many camera-based detectors identify objects reasonably

well. The issue is rooted in these detectors often poorly estimating depth. Common metrics, such as the 3D Average Precision (3D AP), rely on the intersection over union (IoU) to associate the prediction boxes with the ground truth boxes. As a result, they may treat reasonable predictions that suffer from these longitudinal localization errors as false positives, leading to lower and less informative scores.

We therefore propose a variant of the 3D AP metric that is more permissive to depth errors. The proposed longitudinal error tolerant metrics, LET-3D-AP and LET-3D-APL, allow longitudinal localization errors up to a given tolerance. Specifically, we define the longitudinal error to be the object localization error along the line of sight between the camera and the ground truth object. The maximum longitudinal error that our metric tolerates is an adjustable percentage of the distance between the camera and the ground truth object.

For each prediction and ground truth pair with tolerable longitudinal error, we correct the longitudinal error by shifting the prediction box along the line of sight between the camera and the center of the prediction box. We then use the resulting corrected box to compute the IoU, which we refer to as the longitudinal error tolerant IoU (LET-IoU). The precision and recall values are then computed by performing a bipartite matching with weights based on the longitudinal affinity and the LET-IoU values.

Finally, we define two longitudinal error tolerant metrics, LET-3D-AP and LET-3D-APL. First, the metric LET-3D-AP is the AP on matching results using proposed method. Note that this metric does not penalize any corrected errors and is therefore comparable to the original 3DAP metric, but with more tolerant matching. In contrast to this, the metric LET-3D-APL penalizes longitudinal localization errors by scaling the precision.

*Work done while at Waymo.

To evaluate the proposed metrics, we extended the existing Waymo Open Dataset [21] by (1) creating a new dedicated testing set of 80 segments (80,000 images) with LiDAR data redacted, (2) providing camera-synchronized 3D box labels for the entire dataset, eliminating the camera/label synchronization gap. Waymo included these extensions as part of the Waymo Open Dataset 3D Camera-Only Detection Challenge. The challenge remains open for submissions, and can be used to benchmark camera-only detection methods.

II. RELATED WORK

Following popular 2D detection benchmarks, such as PASCAL VOC [22] and COCO [23], most 3D object detection benchmarks rely on the metric 3D AP to evaluate detections based on the intersection over union (IoU), either in 3D or in a bird’s eye view (BEV), with predefined IoU thresholds. For example, the KITTI dataset [24] and the Waymo Open Dataset [21] adopt 3D IoU as the main matching function. The Waymo Open Dataset proposes to use a heading accuracy weighted AP, referred to as APH, as the primary metric to penalize incorrect heading prediction. NuScenes [25] uses the center distance between predicted objects and ground truth objects as the true positive matching criterion and proposes a set of true positive metrics to quantify other errors, including localization, scale, and orientation.

While LiDAR-based detectors [1]–[7] remain the most popular methods for 3D object detection for autonomous driving, monocular camera-based 3D object detection has been gaining traction in recent years. Methods can be roughly categorized into two groups: 1) The first camp leverages mature perspective 2D detectors and equips the networks with 3D box attributes for 3D detection [8]–[14], [26]–[30]. An emerging direction is to leverage Transformer models for implicit depth encoding [17], [31]–[34]. 2) The second camp leverages mature LiDAR detectors and projects 2D perspective features into 3D in the form of point clouds [16], [20], [35]–[40], feature maps in bird’s eye view (BEV) [15]–[17], [41]–[52], or in voxel space [18], [19], [53], [54]. These methods then predict the detections by applying 3D detection heads to the 3D/BEV feature maps. Accurate monocular depth estimation is essential for all methods. Since monocular depth estimation is intrinsically an ill-posed problem, however, it is difficult for camera-based methods to accurately estimate the depth that corresponds to the objects, resulting in longitudinal localization errors that lead to reduced 3D AP scores when compared to LiDAR-based methods.

As pointed out by Ma *et al.* [55], the performance of monocular camera 3D detection methods can be greatly improved when their longitudinal localization errors are mitigated by using ground truth depth or localization. This is why we are proposing longitudinal error tolerant (LET) metrics for evaluating camera-only 3D detection methods. While generalized intersection over union (GIoU) [56] and its 3D variant [57] can also be used to match non-overlapping bounding boxes, they do not target errors in a specific direction, and the shape and heading mismatch is not factored into the non-overlapping cases.

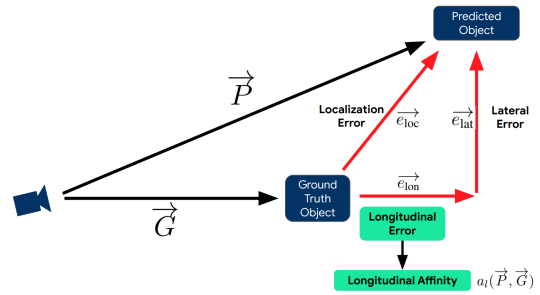


Fig. 2. **Breakdown of the localization error.** We decompose the 3D detection localization error into a lateral error and a longitudinal error. We find that the longitudinal error is more prominent in camera-only 3D detection. We therefore propose longitudinal error tolerant (LET) metrics that are more permissive with respect to the longitudinal localization error.

III. LONGITUDINAL ERROR TOLERANT 3D AP

The 3D AP metric relies on the IoU to match prediction boxes with ground truth boxes. Therefore, prediction boxes that have little or no overlap with the corresponding ground truth boxes will be treated as false positives. However, these predictions may still contribute valuable information to the decision making of an autonomous driving system. We therefore propose a metric that rewards such detections.

Our proposed metrics are inspired by the following objectives: First, given a model of an assumed localization error distribution, design a new matching criterion so that a predicted box may still match with a target ground truth box even when they do not match in terms of IoU. Second, design a new bipartite matching cost function that takes the localization, shape, and heading errors into account so that frame-level matching can be properly calculated. Last, design a penalty term to penalize detections that can only be matched with the ground truth when using the longitudinal error tolerant matching.

A. Localization Errors in Camera-Based 3D Detection

We assume a ground truth bounding box G with center $\vec{g} \in \mathcal{R}^3$ and a predicted bounding box P with center $\vec{p} \in \mathcal{R}^3$ such that the origin $[0, 0, 0]$ is the camera location, or a mean position in the case of multi-camera setup. That is, all 3D location vectors are in the camera frame. We define the localization error as the vector

$$\vec{e}_{loc} = \vec{p} - \vec{g}. \quad (1)$$

We decompose the localization error into two components: noitemsep

- The longitudinal error \vec{e}_{lon} is the error along the line of sight from the center of the prediction box to the center of the ground truth box, giving $\vec{e}_{lon} = (\vec{e}_{loc} \cdot \vec{u}_G) \cdot \vec{u}_G$, where $\vec{u}_G = \vec{g}/|\vec{g}|$ is the unit vector of \vec{g} .
- The lateral error \vec{e}_{lat} is the distance between the predicted box P and the line of sight to the ground truth box G . It is defined as the shortest distance from the predicted box to any point on the line of sight, leading to $\vec{e}_{lat} = \vec{e}_{loc} - \vec{e}_{lon}$.

Figure 2 illustrates the error terms. We observe that localization errors tend to have the following attributes for

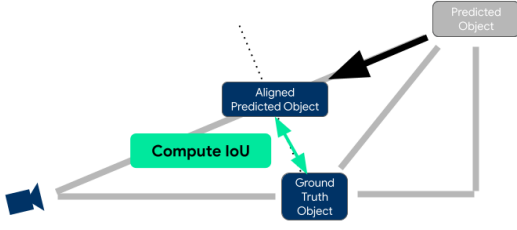


Fig. 3. **Computing LET-IoU.** Given a predicted object and a ground truth object to be matched with, we move the predicted object along the line of sight to obtain minimal distance to the ground truth center. We then compute the LET-IoU as the 3D-IoU between the aligned predicted object and the ground truth object.

camera-based 3D detectors. Localization errors tend to be the most pronounced along the line of sight because of imperfect depth estimation. We assume that the standard deviation of the longitudinal error, \vec{e}_{lon} , is proportional to the distance between the sensor and the center of the ground truth bounding box, \vec{g} . The lateral error, \vec{e}_{lat} , is the result of an imperfect estimation of the object center on the camera image plane. Since the size of the bounding box projected onto the camera plane is inversely proportional to the range to a given ground truth, G , the standard deviation of the center estimation error in pixels, $\sigma(|\vec{e}_{\text{cam}}|)$, is also inversely proportional to the range of a given ground truth \vec{g} , that is, $\sigma(|\vec{e}_{\text{cam}}|) \propto 1/|\vec{g}|$. The lateral error in 3D space, however, is scaled by the range projection, that is, $\vec{e}_{\text{lat}} = |\vec{g}| \cdot \sigma(|\vec{e}_{\text{cam}}|)$. Therefore, the standard deviation of the lateral error is independent of the range of the ground truth object and can be set as a constant. We therefore only introduce a tolerance for the longitudinal localization errors.

B. Longitudinal Affinity

We propose a scalar value, longitudinal affinity $a_l(\vec{p}, \vec{g})$, to determine the scores for matching prediction boxes with ground truth boxes given a tolerance for the longitudinal error. Specifically, the longitudinal affinity, whose value is in $[0.0, 1.0]$, estimates how well the centers of a prediction box and the ground truth box align. Given the longitudinal error, \vec{e}_{lon} , between a pair of prediction and ground truth, we define the longitudinal affinity based on the following hyperparameters: noitemsep

- longitudinal_tolerance_percentage T_l^p : The maximum longitudinal error \vec{e}_{lon} is expressed as a percentage T_l^p of the range to the ground truth G . For example, $T_l^p = 0.1$ provides a 10% tolerance, and for a ground truth object that is 50 meters away ($|\vec{g}| = 50$), the longitudinal tolerance is 5 meters.
- min_longitudinal_tolerance_meter T_l^m : When a ground truth object is close to the sensor origin, the percentage-based tolerance can result in a small matching region. This parameter controls the minimum absolute tolerance, thus mainly affecting near range objects.

Finally, we define the longitudinal affinity $a_l(\vec{p}, \vec{g})$ between a prediction box with center \vec{p} and a ground truth box with

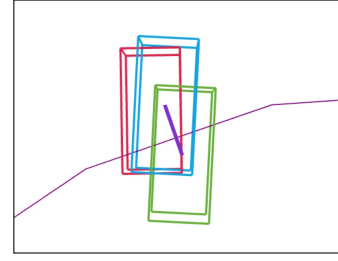


Fig. 4. **An example of a matched detection using LET-IoU.** The green box denotes the detection, the red box denotes the ground truth, and the blue box denotes the longitudinal aligned detection as stated in Section III-C. We also show the connections between matched prediction boxes and aligned boxes using a purple connector.

center \vec{g} as:

$$a_l(\vec{p}, \vec{g}) = 1 - \min\left(\frac{|\vec{e}_{\text{lon}}(\vec{p}, \vec{g})|}{T_l}, 1.0\right), \quad (2)$$

where $T_l = \max(T_l^p \cdot |\vec{g}|, T_l^m)$.

C. LET-IoU: Logitudinal Error Tolerant IoU

The longitudinal affinity captures the longitudinal error of a prediction based on the center of the predicted bounding box and the center of the ground truth bounding box. To determine whether a prediction can be associated with a ground truth, we also want to take into account the shape, size, and heading error. When relying on the regular 3D AP, this is only captured by 3D IoU. We propose LET-IoU, where IoU is calculated between the ground truth bounding box and the prediction bounding box after compensating for the longitudinal error. Specifically, we mitigate the longitudinal error of the prediction by aligning its center along the line of sight with the ground truth.

Given a ground truth with center \vec{g} and a prediction with center \vec{p} , the objective is to move the center location of the prediction box along the line of sight so that the IoU between the moved prediction box and the ground truth box is maximized:

$$\vec{p}_{\text{aligned}} = \underset{P_{\text{aligned}}}{\operatorname{argmax}} \quad 3\text{D-IoU}(P_{\text{aligned}}, G), \quad (3)$$

where P_{aligned} is the prediction box P with updated center \vec{p}_{aligned} . However, there is no closed-form solution to (3), and exhaustive search along the line of sight is computationally expensive. We therefore approximate the objective by minimizing the distance between the moved prediction box center and the ground truth center, where the longitudinal error is compensated. In other words, the center of the aligned prediction is the projection of the ground truth center \vec{g} onto the line of sight from the sensor to the prediction object, leading to

$$\vec{p}_{\text{aligned}} = (\vec{g} \cdot \vec{u}_P) \cdot \vec{u}_P, \quad (4)$$

where $\vec{u}_P = \vec{p}/|\vec{p}|$ is the unit vector along the line of sight to prediction center \vec{p} . A detailed analysis on the quality of approximation (4) can be found in the supplementary material.

Finally, we obtain the LET-IoU by calculating the typical 3D IoU between the aligned prediction box P_{aligned} and the target ground truth box G , giving

$$\text{LET-IoU}(P, G) = 3\text{D-IoU}(P_{\text{aligned}}, G). \quad (5)$$

See Figure 3 for an illustration. Note that for simplicity, this function does not assume that the longitudinal error is within a given tolerance. In the final metrics computation, LET-IoU will only be calculated on pairs with non-negative longitudinal affinity, where $a_l > 0$.

Figure 4 shows that the prediction (green) is aligned to the target ground truth (red), where the 3D IoU is computed between the aligned prediction (yellow) and the ground truth, resulting in 0.7 LET-IoU.

D. Bipartite Matching with Longitudinal Error Tolerance

To calculate the precision and recall values, detection metrics need to perform a bipartite matching between the prediction set and the ground truth set. Most bipartite matching algorithms involve computing an association weight matrix $W \in \mathcal{R}^{N_P \times N_G}$, where N_P and N_G are the numbers of detections and ground truth objects. The objective is to maximize the summed weights among all the matched pairs. We may take into consideration the longitudinal error, the shape error, and potentially the heading error.

The typical matching weight function in 3D AP computes the IoU between a prediction box and a ground truth box with an IoU threshold T_{iou} :

$$W(i, j) = \begin{cases} \text{IoU}(P(i), G(j)), & \text{if } \text{IoU}(P(i), G(j)) > T_{\text{iou}} \\ 0, & \text{otherwise} \end{cases}, \quad (6)$$

where P and G are the prediction box set and ground truth box set for a single frame, respectively. However, in our setting, there are two affinity terms to be considered: longitudinal affinity a_l and LET-IoU. As a result, we propose to calculate the bipartite matching weight where both terms are taken into account:

$$W(i, j) = \begin{cases} a_l \cdot \text{LET-IoU}, & \text{if } a_l > 0 \\ & \text{and LET-IoU} > T_{\text{iou}}, \\ 0, & \text{otherwise} \end{cases}, \quad (7)$$

where we omit the function input terms $(P(i), G(j))$ of a_l and LET-IoU for simplicity. This allows us to take the shape and heading error into account while prioritizing the detections that have higher longitudinal affinity.

After computing the matching weight matrix, we run a bipartite matching method (Greedy or Hungarian) to compute the matching results, including matched pairs (true positives / TP), non-matched predictions (false positives / FP), and non-matched ground truths (false negatives / FN).

E. LET-3D-AP and LET-3D-APL

a) LET-3D-AP: Average Precision with Longitudinal Error Tolerance.: Once the matching results are finalized, each matched prediction will be counted as a true positive (TP). A prediction without matching ground truth is counted as a false positive (FP). If a ground truth is not matched with any prediction, the ground truth is counted as a false negative

(FN). Then the precision $p = |TP|/(|TP| + |FP|)$ and recall $r = |TP|/(|TP| + |FN|)$ can be calculated. After computing the precision and recall values for detection subsets with different score cutoffs, a PR curve can be obtained. Finally, the LET-3D-AP is calculated from the average precision of the PR curve: $\text{LET-3D-AP} = \int_0^1 p(r)dr$, where $p(r)$ is the precision value at recall r .

Here, we do not penalize depth errors when computing the PR curve, even though we may have had to adjust some predictions to compensate for their depth errors. This provides a number comparable to 3D AP but with a more tolerant matching criterion.

b) LET-3D-APL: Longitudinal Affinity Weighted LET-3D-AP.: Here, we penalize those predictions that do not overlap with any ground truth, that is, those which only match a ground truth bounding box owing to the above-mentioned center alignment. We penalize these predictions by using the longitudinal affinity $a_l(\vec{p}, \vec{g})$ proposed above. To this end, we propose a weighted variant of precision values.

Though the number of true positives $|TP|$ is used both in the precision and recall computation, they represent different ideas. In precision calculation, $|TP_P|$ means the number of matched predictions, while in the recall calculation, $|TP_G|$ means the number of matched ground truths. As a result, we rewrite the precision and recall as

$$\text{Precision} = \frac{|TP_P|}{|TP_P| + |FP|} \quad (8)$$

$$\text{Recall} = \frac{|TP_G|}{|TP_G| + |FN|} \quad (9)$$

to emphasize the difference between the prediction accumulator and the ground truth accumulator.

In the precision computation, we traverse through the predictions to accumulate the FP 's and TP 's. For any unmatched prediction, it only contributes to the FP -accumulators with 1.0. However, for a matched prediction P with respect to a ground truth \vec{g} , it contributes to TP -accumulator with the quantity of $a_l(\vec{p}, \vec{g})$ and also contributes to the FP -accumulator with the quantity of $1 - a_l(\vec{p}, \vec{g})$. Essentially, we distribute part of the TP -accumulator to the FP -accumulator based on the longitudinal affinity. Then, the soft TP - and FP -accumulators are:

$$|TP_P| = \sum_{\text{matched } P} a_l(\vec{p}, \vec{g}) \quad (10)$$

$$|FP| = \sum_{\text{matched } P} (1 - a_l(\vec{p}, \vec{g})) + \sum_{\text{unmatched } P} 1.0 \quad (11)$$

Based on the definition of soft TP and FP , the soft precision can then be computed as:

$$\text{Prec}_L = \frac{|TP_P|}{|TP_P| + |FP|} = \bar{a}_l \cdot \text{Precision} \quad (12)$$

which results in a mean longitudinal affinity weighted precision point.

For the recall computation, we propose to not weight the TP_G since the ground truth does get matched, and there is no reason to penalize the metric twice. As a result, the

precision values are discounted by the multiplier \bar{a}_l , which is the average longitudinal affinity of all the matched predictions that was treated as TP .

Finally, the LET-3D-APL can be calculated with the longitudinal affinity weighted PR curve:

$$\text{LET-3D-APL} = \int_0^1 \text{Prec}_L(r) dr = \int_0^1 \bar{a}_l \cdot \text{Prec}(r) dr, \quad (13)$$

where $\text{Prec}_L(r)$ is the longitudinal affinity weighted precision, and $\text{Prec}(r)$ is the precision at recall r . Note that the weight $a_l(\vec{p}, \vec{g})$ depends on the specific score cutoff at the PR point and therefore cannot be taken out of the integral.

IV. CAMERA-PRIMARY 3D DETECTION DATASET

To evaluate the proposed LET metrics, we extend the existing Waymo Open Dataset [21]. Our contributions are two-fold: (1) We provide a dedicated test set of 80 segments with LiDAR sensor data redacted, (2) We significantly improve camera/label synchronization throughout the dataset. Waymo conducted the Waymo Open Dataset 3D Camera-Only Detection Challenge[†] between April and May 2022, with LET-3D-APL being the primary metric for determining the winning submissions.

Our dedicated test set contains 80 segments in the same format as the original dataset release (20s, 10Hz, 5 cameras), for a total of 1,000 camera images per segment and 80,000 images overall. LiDAR sensor data was used during labeling to ensure high-quality 3D boxes, but redacted before the release to ensure compliance with the dataset challenge rule with regards to basing predictions solely on cameras.

The original Waymo Open Dataset has a synchronization gap of $[-6, 7]$ ms between camera and LiDAR sensor data [21]. Since the 3D object labels are based on LiDAR sensor data, this gap translates into a corresponding synchronization gap between camera and LiDAR-based labels. Motion of the ego-vehicle and independent object motion can lead to misaligned labels with respect to the camera point of view.

To address this issue, we add a new field `CAMERA_SYNCED_BOX`, a variant of `BOX`, which is adjusted to eliminate the synchronization gap to the camera that perceives it. The adjustment is based on solving an optimization problem that takes into account the camera rolling shutter, the motion of the autonomous vehicle and the motion of the object of interest.

Figure 5 visualizes statistics of the box shift. The analysis suggests that, in practice, the shift highly depends on the camera type, with the side-facing cameras benefiting the most from improved synchronization as they are oriented orthogonally to the direction of motion and as they tend to observe close-by objects. In terms of object categories, the shift is the least pronounced for pedestrians, and the most pronounced for vehicles. This is due to pedestrians moving more slowly, reducing displacement through independent object motion, and being predominantly present in low-speed areas, reducing displacement through ego-motion.

[†]<https://waymo.com/open/challenges/2022/3d-camera-only-detection>

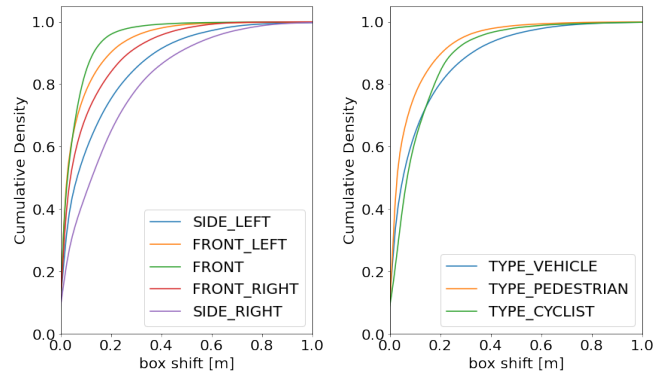


Fig. 5. **CDFs of Box Shifts.** We visualize the shift between `BOX` and `CAMERA_SYNCED_BOX` based on camera types (left) and select object types (right) on the validation set.

A. Comparison to Other Datasets

Table I shows a comparison of popular real-world AV datasets with an emphasis on camera data and synchronization properties. Two traditional datasets in particular, KITTI [24] and Cityscapes 3D [58], are restricted by the dataset size, as well as a limited number of cameras, only spanning a comparatively small field of view. Datasets such as Lyft [60] and nuScenes [25] offer multiple camera views but can experience a synchronization gap of roughly 5 – 10ms, depending on the object location on the image plane. For nuScenes, it is also worth pointing out that the displacement between the laser and camera sensors is more significant than in other datasets, ranging from 0.56 – 0.93m. This viewpoint discrepancy makes accurate camera visibility filtering more difficult.

Both Argoverse 2 Sensor [59] and the newly extended Waymo Open Dataset are large-scale datasets that offer good synchronization. A strength of the Argoverse 2 Sensor dataset is the availability of even more surround view cameras, capturing a whole 360 degrees. A strength of the Waymo Open Dataset lies in the synergies found in many additional label modalities, including camera-based bounding boxes, human keypoints and video panoptic segmentation labels, as well as additional 3D label modalities.

V. EXPERIMENTAL RESULTS

In this section, we analyze the proposed LET metrics against both LiDAR-based and camera-only 3D detectors.

A. Evaluation Dataset and Baseline Methods

To verify the proposed LET metrics, we evaluate two LiDAR-based detectors and two camera-only 3D detectors trained on the Waymo Open Dataset [21] (WOD) and report metrics on the newly proposed test set.

SWFormer [61]: A state-of-the-art LiDAR-based 3D detector that builds upon the idea of Swin Transformer [62] and operates on sparse voxels. It achieves 73.36 L2 vehicle mAPH on the WOD original test set.

PointPillars [3]: A well-established LiDAR-based 3D detector baseline that achieves 60.05 L2 vehicle mAPH on the WOD original test set.

Dataset	KITTI [24]	Cityscapes 3D [58]	Argoverse 2 [59]	Lyft [60]	nuScenes [25]	Extended WOD [21]
# Frames	15K	5K	150K	55K	40K	216K
# Cameras	2	2	9	7	6	5
# Surround View	1	1	7	6	6	5
Camera Shutter Type	Global	Rolling	Global	Global	Global	Rolling
Resolution [MP]	0.7	2.1	3.1	1.3 / 2.1	1.4	2.5
Sync Gap [ms]	[-12.5, 12.5]	0*	[-1.39, 1.39]	[-9.7, 9.7]	[-4.9, 4.9]	0*
Cam ↔ Label Center						
Label Types**	3D Bounding Box 3D Optical Flow 2D Camera Box 2D Panoptic Seg	3D Bounding Box 2D Panoptic Seg	3D Bounding Box	3D Bounding Box	3D Bounding Box 3D Semantic Seg	3D Bounding Box 3D Semantic Seg 3D Human Keypoints 2D Camera Box 2D Human Keypoints 2D Video Panoptic Seg

TABLE I. **Comparison of Popular Real-World AV Datasets.** We only count fully 3D box labeled frames and define a frame as representing a collection of all respective camera images in one instance. The original Waymo Open Dataset sync gap was $[-6, 7]$ ms and is now effectively reduced to 0ms. The sync gaps of other datasets depend on the horizontal object position in the image plane and falls within the given range. *Cityscapes 3D is labeled on the stereo camera imagery directly, while our CAMERA_SYNCED_BOX field is the result of our optimization method, which undoes the label center sync gap considering both egomotion and independent object motion. **Some label types are only available for a subset of the data.

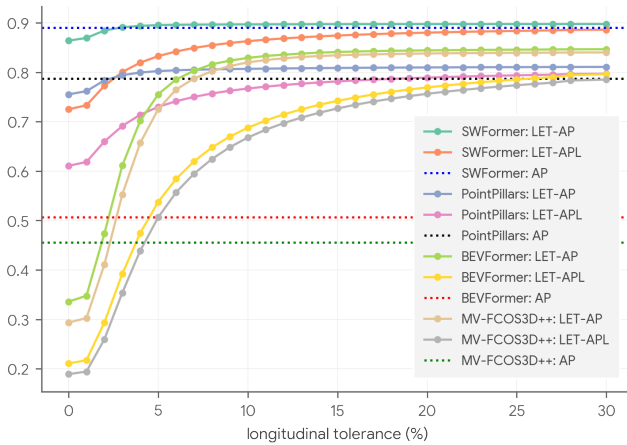


Fig. 6. **LET metrics with different longitudinal error tolerance values.** We show the LET-3D-AP and LET-3D-APL, as well as the original 3D AP of the selected LiDAR-based detector (SWFormer, PointPillars) and camera-based detectors (BEVFormer, MV-FCOS3D++) on the proposed new test set. Higher tolerances lead to higher scores since more detections are being matched with ground truth objects. Surprisingly, despite BEVFormer having absolute 30% lower 3D AP than PointPillars, it outperforms PointPillars with LET-3D-AP(L) metrics past a 10% tolerance. This suggests that existing camera-based detectors have the potential to surpass LiDAR-based detectors, especially in downstream applications, provided that (minor) localization errors are tolerated. Also, LET-3D-APL provides a smoother transition for different tolerance values and is thus more suitable for comparing camera-based 3D detectors.

BEVFormer [41]: A camera-only 3D detector that learns unified BEV representations with spatio-temporal transformers to tackle both 3D detection and segmentation tasks. The method achieves state-of-the-art performance on nuScenes [25] and WOD. We evaluate a specific variant of BEVFormer that won the 2022 Waymo Open Dataset 3D Camera-Only Detection Challenge.

MV-FCOS3D++ [30]: A camera-only 3D detector that adds 2D supervision and temporal information onto the BEV style detector and achieves 2nd place in the 2022 Waymo Open Dataset 3D Camera-Only Detection Challenge.

B. Comparisons of Longitudinal Tolerance Values

The main hyperparameter of the proposed metrics is longitudinal_tolerance_percentage T_l^p . We show the performance of the LiDAR-based detectors (SWFormer, PointPillars) and camera-only detectors (BEVFormer, MV-FCOS3D++) with different tolerance values in Figure 6 for the vehicle class.

As shown in Figure 6, higher longitudinal error tolerance leads to higher LET-3D-AP and LET-3D-APL because more ground truth objects are matched with detections. Note that for the LiDAR-based detectors, LET-AP remains similar to the AP values for all longitudinal tolerance values since the longitudinal errors of LiDAR-based detections are already small. The results also suggest that the proposed LET metrics do not introduce additional matching errors and can reliably evaluate LiDAR-based detectors as well.

To compute LET metrics, a longitudinal tolerance value must be chosen, and the choice of the downstream modules, e.g. tracking or behavior prediction, especially for an autonomous driving system. Users can also sweep the tolerance values to gain more understanding of the error patterns.

C. LET-AP v.s. AP

We compare the proposed LET-AP and LET-APL metrics with AP on the selected baselines and show results in Figure 6. For the LiDAR-based detectors (SWFormer, PointPillars), we show that LET-AP is mostly consistent with AP, which suggests that the matching results are similar in the presence of longitudinal tolerance. For higher tolerance values, LET-3D-AP is slightly higher than 3D AP due to the small amount of additional detections being matched with ground truth objects with more error tolerance. Also, due to the accuracy of LiDAR range estimates, the boxes are fairly accurate, resulting in minimal difference between LET-AP and LET-APL since the allowed longitudinal tolerance is not used by most matching pairs.

The LET-AP metrics results of the camera-only detectors in Figure 6 exhibit a much larger gap to the AP baseline. This shows that many detections can be properly matched to ground

Method	Metrics	Class				Range (Vehicle)		
		All	Vehicle	Pedestrian	Cyclist	[0, 30)	[30, 50)	[50, ∞)
SWFormer	3D AP (%)	N/A	89.0	86.7	N/A	96.0	89.5	78.7
	LET-3D-AP (%)	N/A	89.7	87.3	N/A	96.2	90.2	79.7
	LET-3D-APL (%)	N/A	86.3	85.4	N/A	91.6	87.9	78.1
	mLA	N/A	0.962	0.978	N/A	0.952	0.975	0.980
PointPillars	3D AP (%)	N/A	78.6	58.3	N/A	88.2	76.4	58.4
	LET-3D-AP (%)	N/A	80.7	62.7	N/A	88.5	78.5	66.2
	LET-3D-APL (%)	N/A	76.7	61.0	N/A	83.0	75.9	54.1
	mLA	N/A	0.950	0.973	N/A	0.938	0.967	0.817
BEVFormer	3D AP (%)	35.3	50.7	22.3	33.0	79.7	47.2	20.5
	LET-3D-AP (%)	70.7	82.9	71.1	58.1	89.7	80.6	50.1
	LET-3D-APL (%)	56.2	68.8	53.2	46.5	75.3	68.5	38.9
	mLA	0.795	0.830	0.748	0.800	0.839	0.850	0.776
MV-FCOS3D++	3D AP (%)	30.3	45.6	16.7	28.5	79.2	37.5	13.0
	LET-3D-AP (%)	66.0	82.1	63.0	53.0	89.3	78.0	66.1
	LET-3D-APL (%)	51.1	66.9	45.0	41.3	74.5	63.6	52.0
	mLA	0.774	0.815	0.714	0.779	0.834	0.815	0.787

TABLE II. **LET metrics of different breakdowns.** The methods are evaluated on the new test set with 80 multi-camera sequences. We report 3D AP, LET-3D-AP, LET-3D-APL, and mean longitudinal affinity (mLA) for all the class and range breakdowns, with 10% of longitudinal tolerance. For the LiDAR-based detector, the proposed metrics show similar performance since most longitudinal tolerance is not used for matching predictions and ground truths. For camera-based detectors, the results show that proposed LET metrics are more suitable for evaluation since predictions can be better matched with ground truths, especially for small objects like pedestrian and long-range detections as indicated by the difference between 3D AP and LET-3D-AP(L).

truth objects with a certain amount of longitudinal tolerance, making the resulting LET-AP(L) metrics better suited for evaluating these methods. Under 10% tolerance, BEVFormer achieves higher metrics than PointPillars, indicating BEVFormer may actually have better downstream performance provided sufficient robustness towards localization errors. Compared to the LiDAR-based detectors, the drop off between LET-AP and LET-APL is larger, demonstrating higher longitudinal error among the true positive examples.

D. Metrics of Different Breakdowns

We show detailed metrics on the proposed new test set in Table II. We report 3D AP, LET-3D-AP, LET-3D-APL, and mean longitudinal affinity (mLA) for all class and range breakdowns, with 10% of longitudinal tolerance. Note that the 3D AP metrics are computed with 0.5, 0.3, 0.3 IoU thresholds for vehicles, pedestrians and cyclists. As shown in Table II, LET-3D-AP values are consistently higher than 3D AP values since more detections are matched with ground truth objects with additional longitudinal tolerance. The difference is especially pronounced for small objects like pedestrians, as well as far-away objects. We also report the mean longitudinal affinity values to show the difference between LET-3D-AP and LET-3D-APL. We observe that methods with higher metrics not only have more valid detections but also have better localization as indicated by higher mLA. We can also verify the assumption of depth errors being roughly proportional to range by checking the consistent mLA values with different range breakdowns. Our results suggest that, under the proposed metrics, some camera-only 3D detectors can already surpass the LiDAR-based detectors.

VI. CONCLUSION

We proposed LET-3D-AP(L) metrics for evaluating camera-only 3D detectors. The tolerance along the longitudinal axis

allows detections to be associated with the ground truth objects despite depth estimation errors. The results show that state-of-the-art camera-based detectors can outperform popular LiDAR-based detectors with our metrics, suggesting that existing camera-based methods have the potential in real-world applications. We also construct a new test set for the Waymo Open Dataset, tailored to camera-only 3D detection methods. We hope the proposed metrics and dataset will help advance the field of camera-only 3D detection by providing a more meaningful indication for method performance.

REFERENCES

- [1] P. Sun, W. Wang, Y. Chai, G. Elsayed, A. Bewley, X. Zhang, C. Sminchisescu, and D. Anguelov, "Rsn: Range sparse net for efficient, accurate lidar 3d object detection," in *CVPR*, 2021.
- [2] S. Shi, C. Guo, L. Jiang, Z. Wang, J. Shi, X. Wang, and H. Li, "Pv-rcnn: Point-voxel feature set abstraction for 3d object detection," in *CVPR*, 2020.
- [3] A. H. Lang, S. Vora, H. Caesar, L. Zhou, J. Yang, and O. Beijbom, "Pointpillars: Fast encoders for object detection from point clouds," in *CVPR*, 2019.
- [4] G. P. Meyer, A. Laddha, E. Kee, C. Vallespi-Gonzalez, and C. K. Wellington, "Lasernet: An efficient probabilistic 3d object detector for autonomous driving," in *CVPR*, 2019.
- [5] C. R. Qi, O. Litany, K. He, and L. J. Guibas, "Deep hough voting for 3d object detection in point clouds," in *ICCV*, 2019.
- [6] Y. Zhou and O. Tuzel, "Voxelnet: End-to-end learning for point cloud based 3d object detection," in *CVPR*, 2018.
- [7] V. A. Sindagi, Y. Zhou, and O. Tuzel, "Mvx-net: Multimodal voxelnet for 3d object detection," in *ICRA*, 2019.
- [8] X. Chen, K. Kundu, Z. Zhang, H. Ma, S. Fidler, and R. Urtasun, "Monocular 3d object detection for autonomous driving," in *CVPR*, 2016.
- [9] G. Brazil and X. Liu, "M3d-rpn: Monocular 3d region proposal network for object detection," in *ICCV*, 2019.
- [10] A. Mousavian, D. Anguelov, J. Flynn, and J. Kosecka, "3d bounding box estimation using deep learning and geometry," in *CVPR*, 2017.
- [11] B. Xu and Z. Chen, "Multi-level fusion based 3d object detection from monocular images," in *CVPR*, 2018.
- [12] A. Simonelli, S. R. Buló, L. Porzi, M. López-Antequera, and P. Kotschieder, "Disentangling monocular 3d object detection," in *ICCV*, 2019, pp. 1991–1999.

- [13] X. Zhou, D. Wang, and P. Krähenbühl, “Objects as points,” *arXiv preprint arXiv:1904.07850*, 2019.
- [14] T. Wang, X. Zhu, J. Pang, and D. Lin, “Fcos3d: Fully convolutional one-stage monocular 3d object detection,” in *ICCV*, 2021.
- [15] C. Reading, A. Harakeh, J. Chae, and S. L. Waslander, “Categorical depth distribution network for monocular 3d object detection,” in *CVPR*, 2021.
- [16] Y. Wang, W.-L. Chao, D. Garg, B. Hariharan, M. Campbell, and K. Q. Weinberger, “Pseudo-lidar from visual depth estimation: Bridging the gap in 3d object detection for autonomous driving,” in *CVPR*, 2019.
- [17] Y. Wang, V. C. Guizilini, T. Zhang, Y. Wang, H. Zhao, and J. Solomon, “Detr3d: 3d object detection from multi-view images via 3d-to-2d queries,” in *CORL*. PMLR, 2022.
- [18] T. Roddick, A. Kendall, and R. Cipolla, “Orthographic feature transform for monocular 3d object detection,” *arXiv preprint arXiv:1811.08188*, 2018.
- [19] D. Rukhovich, A. Vorontsova, and A. Konushin, “Imvoxelnet: Image to voxels projection for monocular and multi-view general-purpose 3d object detection,” in *WACV*, 2022.
- [20] J.-J. Hwang, H. Kretschmar, J. Manela, S. Rafferty, N. Armstrong-Crews, T. Chen, and D. Anguelov, “Cramnet: Camera-radar fusion with ray-constrained cross-attention for robust 3d object detection,” in *ECCV*, 2022.
- [21] P. Sun, H. Kretschmar, X. Dotiwala, A. Chouard, V. Patnaik, P. Tsui, J. Guo, Y. Zhou, Y. Chai, B. Caine *et al.*, “Scalability in perception for autonomous driving: Waymo open dataset,” in *CVPR*, 2020.
- [22] M. Everingham, S. Eslami, L. Van Gool, C. K. Williams, J. Winn, and A. Zisserman, “The pascal visual object classes challenge: A retrospective,” *IJCV*, 2015.
- [23] T.-Y. Lin, M. Maire, S. Belongie, J. Hays, P. Perona, D. Ramanan, P. Dollár, and C. L. Zitnick, “Microsoft coco: Common objects in context,” in *ECCV*, 2014.
- [24] A. Geiger, P. Lenz, and R. Urtasun, “Are we ready for autonomous driving? the kitti vision benchmark suite,” in *CVPR*, 2012.
- [25] H. Caesar, V. Bankiti, A. H. Lang, S. Vora, V. E. Liong, Q. Xu, A. Krishnan, Y. Pan, G. Baldan, and O. Beijbom, “nuscenes: A multimodal dataset for autonomous driving,” *arXiv preprint arXiv:1903.11027*, 2019.
- [26] L. Liu, C. Wu, J. Lu, L. Xie, J. Zhou, and Q. Tian, “Reinforced axial refinement network for monocular 3d object detection,” in *ECCV*, 2020.
- [27] A. Simonelli, S. R. Bulo, L. Porzi, E. Ricci, and P. Kotschieder, “Towards generalization across depth for monocular 3d object detection,” in *ECCV*, 2020.
- [28] Y. Chen, L. Tai, K. Sun, and M. Li, “Monopair: Monocular 3d object detection using pairwise spatial relationships,” in *CVPR*, 2020.
- [29] P. Li, H. Zhao, P. Liu, and F. Cao, “Rtm3d: Real-time monocular 3d detection from object keypoints for autonomous driving,” in *ECCV*, 2020.
- [30] T. Wang, Q. Lian, C. Zhu, X. Zhu, and W. Zhang, “Mv-fcos3d++: Multi-view camera-only 4d object detection with pretrained monocular backbones,” *arXiv preprint arXiv:2207.12716*, 2022.
- [31] Y. Liu, T. Wang, X. Zhang, and J. Sun, “Petr: Position embedding transformation for multi-view 3d object detection,” in *ECCV*, 2022.
- [32] K.-C. Huang, T.-H. Wu, H.-T. Su, and W. H. Hsu, “Monodtr: Monocular 3d object detection with depth-aware transformer,” in *Proceedings of the IEEE/CVF Conference on Computer Vision and Pattern Recognition*, 2022, pp. 4012–4021.
- [33] R. Zhang, H. Qiu, T. Wang, X. Xu, Z. Guo, Y. Qiao, P. Gao, and H. Li, “Monodetr: Depth-aware transformer for monocular 3d object detection,” *arXiv preprint arXiv:2203.13310*, 2022.
- [34] Y. Liu, J. Yan, F. Jia, S. Li, Q. Gao, T. Wang, X. Zhang, and J. Sun, “Petrv2: A unified framework for 3d perception from multi-camera images,” *arXiv preprint arXiv:2206.01256*, 2022.
- [35] X. Ma, S. Liu, Z. Xia, H. Zhang, X. Zeng, and W. Ouyang, “Rethinking pseudo-lidar representation,” in *ECCV*, 2020.
- [36] Y. You, Y. Wang, W.-L. Chao, D. Garg, G. Pleiss, B. Hariharan, M. Campbell, and K. Q. Weinberger, “Pseudo-lidar++: Accurate depth for 3d object detection in autonomous driving,” *arXiv preprint arXiv:1906.06310*, 2019.
- [37] M. Ding, Y. Huo, H. Yi, Z. Wang, J. Shi, Z. Lu, and P. Luo, “Learning depth-guided convolutions for monocular 3d object detection,” in *CVPR workshops*, 2020.
- [38] R. Qian, D. Garg, Y. Wang, Y. You, S. Belongie, B. Hariharan, M. Campbell, K. Q. Weinberger, and W.-L. Chao, “End-to-end pseudo-lidar for image-based 3d object detection,” in *Proceedings of the IEEE/CVF Conference on Computer Vision and Pattern Recognition*, 2020, pp. 5881–5890.
- [39] Y. Chen, S. Liu, X. Shen, and J. Jia, “Dsgn: Deep stereo geometry network for 3d object detection,” in *Proceedings of the IEEE/CVF conference on computer vision and pattern recognition*, 2020, pp. 12 536–12 545.
- [40] X. Guo, S. Shi, X. Wang, and H. Li, “Liga-stereo: Learning lidar geometry aware representations for stereo-based 3d detector,” in *Proceedings of the IEEE/CVF International Conference on Computer Vision*, 2021, pp. 3153–3163.
- [41] Z. Li, W. Wang, H. Li, E. Xie, C. Sima, T. Lu, Q. Yu, and J. Dai, “Bevformer: Learning bird’s-eye-view representation from multi-camera images via spatiotemporal transformers,” in *ECCV*, 2022.
- [42] X. Weng and K. Kitani, “Monocular 3d object detection with pseudo-lidar point cloud,” in *ICCV Workshops*, 2019.
- [43] J. Huang, G. Huang, Z. Zhu, and D. Du, “Bevdet: High-performance multi-camera 3d object detection in bird-eye-view,” *arXiv preprint arXiv:2112.11790*, 2021.
- [44] Y. Li, Z. Ge, G. Yu, J. Yang, Z. Wang, Y. Shi, J. Sun, and Z. Li, “Bevdepth: Acquisition of reliable depth for multi-view 3d object detection,” *arXiv preprint arXiv:2206.10092*, 2022.
- [45] E. Xie, Z. Yu, D. Zhou, J. Philion, A. Anandkumar, S. Fidler, P. Luo, and J. M. Alvarez, “M² bev: Multi-camera joint 3d detection and segmentation with unified birds-eye view representation,” *arXiv preprint arXiv:2204.05088*, 2022.
- [46] Y. Jiang, L. Zhang, Z. Miao, X. Zhu, J. Gao, W. Hu, and Y.-G. Jiang, “Polarformer: Multi-camera 3d object detection with polar transformers,” *arXiv preprint arXiv:2206.15398*, 2022.
- [47] Z. Liu, H. Tang, A. Amini, X. Yang, H. Mao, D. Rus, and S. Han, “Bevfusion: Multi-task multi-sensor fusion with unified bird’s-eye view representation,” *arXiv preprint arXiv:2205.13542*, 2022.
- [48] J. Huang and G. Huang, “Bevdet4d: Exploit temporal cues in multi-camera 3d object detection,” *arXiv preprint arXiv:2203.17054*, 2022.
- [49] Y. Zhang, Z. Zhu, W. Zheng, J. Huang, G. Huang, J. Zhou, and J. Lu, “Beverse: Unified perception and prediction in birds-eye-view for vision-centric autonomous driving,” *arXiv preprint arXiv:2205.09743*, 2022.
- [50] Z. Chen, Z. Li, S. Zhang, L. Fang, Q. Jiang, and F. Zhao, “Graph-detr3d: Rethinking overlapping regions for multi-view 3d object detection,” *arXiv preprint arXiv:2204.11582*, 2022.
- [51] S. Chen, X. Wang, T. Cheng, Q. Zhang, C. Huang, and W. Liu, “Polar parametrization for vision-based surround-view 3d detection,” *arXiv preprint arXiv:2206.10965*, 2022.
- [52] W. Roh, G. Chang, S. Moon, G. Nam, C. Kim, Y. Kim, S. Kim, and J. Kim, “Ora3d: Overlap region aware multi-view 3d object detection,” *arXiv preprint arXiv:2207.00865*, 2022.
- [53] T. Wang, J. Pang, and D. Lin, “Monocular 3d object detection with depth from motion,” in *ECCV*, 2022.
- [54] J. Lu, Z. Zhou, X. Zhu, H. Xu, and L. Zhang, “Learning ego 3d representation as ray tracing,” *arXiv preprint arXiv:2206.04042*, 2022.
- [55] X. Ma, Y. Zhang, D. Xu, D. Zhou, S. Yi, H. Li, and W. Ouyang, “Delving into localization errors for monocular 3d object detection,” in *CVPR*, 2021.
- [56] H. Rezatofoghi, N. Tsoi, J. Gwak, A. Sadeghian, I. Reid, and S. Savarese, “Generalized intersection over union,” in *CVPR*, 2019.
- [57] J. Xu, Y. Ma, S. He, and J. Zhu, “3d-giou: 3d generalized intersection over union for object detection in point cloud,” *Sensors*, 2019.
- [58] N. Gähler, N. Jourdan, M. Cordts, U. Franke, and J. Denzler, “Cityscapes 3d: Dataset and benchmark for 9 dof vehicle detection,” *arXiv preprint arXiv:2006.07864*, 2020.
- [59] B. Wilson, W. Qi, T. Agarwal, J. Lambert, J. Singh, S. Khandelwal, B. Pan, R. Kumar, A. Hartnett, J. K. Pontes *et al.*, “Argoverse 2: Next generation datasets for self-driving perception and forecasting,” in *Thirty-fifth Conference on Neural Information Processing Systems Datasets and Benchmarks Track (Round 2)*, 2021.
- [60] R. Kesten, M. Usman, J. Houston, T. Pandya, K. Nadhamuni, A. Ferreira, M. Yuan, B. Low, A. Jain, P. Ondruska, S. Omari, S. Shah, A. Kulkarni, A. Kazakova, C. Tao, L. Platinsky, W. Jiang, and V. Shet, “Level 5 perception dataset 2020,” <https://level-5-global/level5/data/>, 2019.
- [61] P. Sun, M. Tan, W. Wang, C. Liu, F. Xia, Z. Leng, and D. Anguelov, “Swformer: Sparse window transformer for 3d object detection in point clouds,” in *ECCV*, 2022.
- [62] Z. Liu, Y. Lin, Y. Cao, H. Hu, Y. Wei, Z. Zhang, S. Lin, and B. Guo, “Swin transformer: Hierarchical vision transformer using shifted windows,” in *CVPR*, 2021.